

A 2% Distance to $z = 0.35$ by Reconstructing Baryon Acoustic Oscillations - I : Methods and Application to the Sloan Digital Sky Survey

Nikhil Padmanabhan¹, Xiaoying Xu², Daniel J. Eisenstein³, Richard Scalzo^{1,4}, Antonio J. Cuesta¹, Kushal T. Mehta², Eyal Kazin^{5,6}

¹ Dept. of Physics, Yale University, 260 Whitney Ave, New Haven, CT 06520

² Steward Observatory, University of Arizona, 933 N. Cherry Ave., Tucson, AZ 85721

³ Harvard-Smithsonian Center for Astrophysics, Harvard University, 60 Garden St., Cambridge, MA 02138

⁴ Research School of Astronomy & Astrophysics, The Australian National University, Mount Stromlo Observatory, Cotter Road, Weston ACT 2611, Australia

⁵ Centre for Astrophysics and Supercomputing, Swinburne University of Technology, P.O. Box 218, Hawthorn, Victoria 3122, Australia

⁶ Center for Cosmology and Particle Physics, New York University, 4 Washington Place, 10003 NY, USA

2 February 2012

ABSTRACT

We apply the reconstruction technique to the clustering of galaxies from the Sloan Digital Sky Survey Data Release 7 (SDSS DR7) Luminous Red Galaxy sample, sharpening the baryon acoustic oscillation (BAO) feature and achieving a 1.9% measurement of the distance to $z = 0.35$. This is the first application of reconstruction of the BAO feature in a galaxy redshift survey. We update the reconstruction algorithm of Eisenstein et al. (2007a) to account for the effects of survey geometry as well as redshift-space distortions and validate it on 160 LasDamas simulations. We demonstrate that reconstruction sharpens the BAO feature in the angle averaged galaxy correlation function, reducing the nonlinear smoothing scale Σ_{nl} from 8.1 Mpc/h to 4.4 Mpc/h. Reconstruction also significantly reduces the effects of redshift-space distortions at the BAO scale, isotropizing the correlation function. This sharpened BAO feature yields an unbiased distance estimate ($< 0.2\%$) and reduces the scatter from 3.3% to 2.1%. We demonstrate the robustness of these results to the various reconstruction parameters, including the smoothing scale, the galaxy bias and the linear growth rate. Applying this reconstruction algorithm to the Sloan Digital Sky Survey (SDSS) Luminous Red Galaxy (LRG) Data Release 7 (DR7) sample improves the significance of the BAO feature in these data from 3.3σ for the unreconstructed correlation function, to 4.2σ after reconstruction. We estimate a relative distance scale D_V/r_s to $z = 0.35$ of 8.88 ± 0.17 , where r_s is the sound horizon and $D_V \equiv (D_A^2 H^{-1})^{1/3}$ is a combination of the angular diameter distance D_A and Hubble parameter H . Assuming a sound horizon of 154.25 Mpc, this translates into a distance measurement $D_V(z = 0.35) = 1.356 \pm 0.025$ Gpc. We find that reconstruction reduces the distance error in the DR7 sample from 3.5% to 1.9%, equivalent to a survey with three times the volume of SDSS.

1 INTRODUCTION

The baryon acoustic oscillation method (hereafter BAO) (see Weinberg et al. 2012 for a review) is a geometrical probe of the expansion rate of the Universe. Sound waves in the baryon-photon plasma are frozen as density fluctuations at recombination, with a characteristic scale set by the sound horizon (Sakharov 1966; Sunyaev & Zeldovich 1970; Peebles & Yu 1970; Bond & Efstathiou 1987, 1984; Hu & Sugiyama 1996; Hu et al. 1997; Eisenstein & Hu 1998). These sound waves manifest themselves as a peak in the matter (and therefore galaxy) correlation function at the scale of the sound horizon (~ 150 Mpc for current concordance cosmolo-

gies) or equivalently as a series of oscillations in the power spectrum. Since the sound horizon is precisely calibrated by cosmic microwave background measurements, BAO measurements may be used as a standard ruler (Tegmark 1997; Goldberg & Strauss 1998; Eisenstein et al. 1998; Efstathiou & Bond 1999), mapping the angular diameter distance (with the ruler aligned perpendicular to the line of sight) and the Hubble parameter (with the ruler parallel to the line of sight) as a function of redshift (Blake & Glazebrook 2003; Hu & Haiman 2003; Linder 2003; Seo & Eisenstein 2003). There have now been multiple detections of the BAO feature in galaxy surveys (Cole et al. 2005; Eisenstein et al. 2005; Blake

et al. 2007; Padmanabhan et al. 2007; Percival et al. 2007; Gaztañaga et al. 2009a,b; Kazin et al. 2010; Percival et al. 2010; Reid et al. 2010; Chuang & Wang 2011; Blake et al. 2011b,a; Beutler et al. 2011; Sawangwit et al. 2011; Blake et al. 2011c; Ho et al. 2012; Seo et al. 2012) and current (Schlegel et al. 2009; Drinkwater et al. 2010; Hill et al. 2008) and planned (Schlegel et al. 2011; Laureijs et al. 2011) BAO surveys are now a mainstay of experimental dark energy programs.

A key feature of the BAO method is the fact that the sound horizon is much larger than the scales relevant for nonlinear evolution and galaxy formation. This scale separation protects the BAO feature from large corrections due to these effects and therefore from systematic errors. There is now a considerable literature quantitatively exploring these effects both using perturbative techniques and simulations (Meiksin et al. 1999; Seo & Eisenstein 2003; Jeong & Komatsu 2006; Huff et al. 2007; Guzik et al. 2007; Eisenstein et al. 2007b; Angulo et al. 2008; Crocce & Scoccimarro 2008; Smith et al. 2008; Seo et al. 2008; Padmanabhan & White 2009; Seo et al. 2010; Mehta et al. 2011) and consensus that systematic effects that might bias distance estimates with the standard ruler are indeed small.

The dominant effect of the nonlinear evolution of the density field is to smooth the BAO feature in the correlation function. This is equivalent to suppressing the oscillations in the power spectrum. While this smoothing does not bias the distance measurements, it does reduce the contrast in the BAO feature and increases the distance errors. This smoothing is well understood (Eisenstein et al. 2007b; Crocce & Scoccimarro 2008; Padmanabhan & White 2009; Matsubara 2008b,a; Seo et al. 2010) and is physically caused by large-scale ($\sim 20\text{Mpc}/h$) flows. This realization led Eisenstein et al. (2007a) to suggest that this smoothing of the BAO feature may be reversed, a process commonly referred to as “reconstruction”. They provide a simple prescription for this process that has been shown to sharpen the BAO feature and improve distance constraints (Padmanabhan et al. 2009; Noh et al. 2009; Seo et al. 2010; Mehta et al. 2011). It is important to emphasize here that this is not a deconvolution but rather uses information beyond the two-point function that exists in the density field.

Although reconstruction has been studied with simulations in the past, the present paper represents the first application to data. The Sloan Digital Sky Survey (SDSS) Luminous Red Galaxy (LRG) sample represents the current state of the art in low-redshift BAO measurements and is a natural sample to implement reconstruction on. This sample was analyzed by Percival et al. (2010) using the power spectrum and Kazin et al. (2010) using the correlation function, who report a $\sim 3.5\%$ distance measurement for the LRG sample alone, and a $\sim 2.7\%$ measurement when combined with a lower redshift sample of galaxies from the SDSS. This work is the natural extension of these previous results. In addition to improving the distance constraints from this sample, the performance of reconstruction on the SDSS has important implications for the expected performance of future surveys, most of which assume some level of reconstruction.

This is the first in a sequence of three papers. This paper describes the details of the reconstruction algorithm used, tests it on simulated data, and then presents the results for the DR7 data. The second paper in this series (Xu et al.

2012, hereafter Paper II) describes how we robustly fit the galaxy correlation function to obtain our distance measurements. The third paper (Mehta et al. 2012, hereafter Paper III) presents the cosmological implications of these measurements.

This paper is structured as follows: § 2 introduces the basic principle behind reconstruction and then presents a detailed description of the algorithm implemented in this work. We describe the data and simulations used in § 3. We discuss the impact of reconstruction on the BAO feature and the derived distances on simulated data in § 4; we then apply it to the data in § 5. We summarize our conclusions in § 6.

2 METHODS

We describe the various algorithms used in the reconstruction of the BAO feature below. We start by describing the physical basis for reconstruction and outline the reconstruction algorithm. We then describe our approach to dealing with survey boundaries, as well as our procedure for estimating a distance scale from a correlation function.

2.1 Understanding Reconstruction

Figure 1 highlights the key aspects of reconstruction. As was first emphasized by Eisenstein et al. (2007b), the erasure of the BAO feature can be physically traced to the pairwise relative velocities of particles separated by $\sim 100\text{Mpc}/h$. Figure 1 highlights this, showing a slice through an N-body simulation, with tracer particles representing the BAO feature highlighted. The dominant smoothing of the BAO feature is due to the coherent flows that form the large-scale structure, not the random motions of particles within gravitational structures. This is the key insight behind reconstruction - the same galaxy surveys used to detect the BAO feature also map the cosmic structure responsible for its erasure. One can therefore use these same surveys to infer the large scale flow field and partially undo the smoothing of the BAO feature.

Figure 1 also makes it clear that reconstruction is actually working at the level of the density field, using information beyond what exists simply in the two-point statistics of the field. The gains of reconstruction therefore *cannot* be achieved by simply forward modeling the correlation function into the nonlinear regime. While one might attempt to recover this information by considering higher order statistics of the density field, this is an awkward encoding of the information required.

The steps outlined in the figures are a simplification of the reconstruction algorithm we use; we describe the detailed algorithm next.

2.2 A Reconstruction Algorithm

We implement an extended version of the reconstruction algorithm of Eisenstein et al. (2007a). The theoretical underpinnings of this algorithm have been described in Padmanabhan et al. (2009) and Noh et al. (2009), and the algorithm has been validated against several different suites of simulations (Seo et al. 2010; Mehta et al. 2011). We outline the

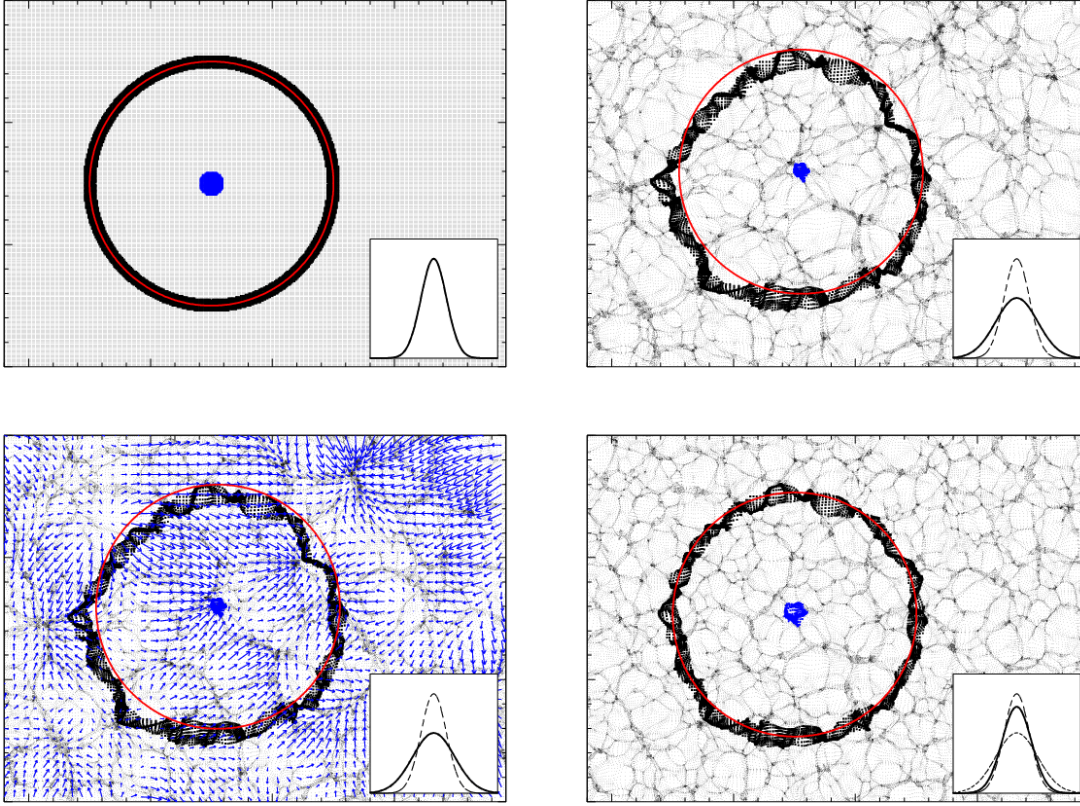


Figure 1. A pictorial explanation of how density-field reconstruction can improve the acoustic scale measurement. In each panel, we show a thin slice of a simulated cosmological density field. (*top left*) In the early universe, the initial densities are very smooth. We mark the acoustic feature with a ring of 150 Mpc radius from the central points. A Gaussian with the same rms width as the radial distribution of the black points from the centroid of the blue points is shown in the inset. (*top right*) We evolve the particles to the present day, here by the Zel’dovich approximation (Zel’dovich 1970). The red circle shows the initial radius of the ring, centered on the current centroid of the blue points. The large-scale velocity field has caused the black points to spread out; this causes the acoustic feature to be broader. The inset shows the current rms radius of the black points relative to the centroid of the blue points (solid line) compared to the initial rms (dashed line). (*bottom left*) As before, but overplotted with the Lagrangian displacement field, smoothed by a $10h^{-1}$ Mpc Gaussian filter. The concept of reconstruction is to estimate this displacement field from the final density field and then move the particles back to their initial positions. (*bottom right*) We displace the present-day position of the particles by the opposite of the displacement field in the previous panel. Because of the smoothing of the displacement field, the result is not uniform. However, the acoustic ring has been moved substantially closer to the red circle. The inset shows that the new rms radius of the black points (solid), compared to the initial width (long-dashed) and the uncorrected present-day width (short-dashed). The narrower peak will make it easier to measure the acoustic scale. Note that the algorithm applied to the data is more complex than was just described, but this figure illustrates the basic opportunity of reconstruction.

steps of this algorithm below and discuss details specific to our implementation in subsequent subsections.

- (i) Estimate the unreconstructed power spectrum $P(k)$ or correlation function $\xi(r)$.
- (ii) Estimate the galaxy bias b and the linear growth rate, $f \equiv d \ln D / d \ln a \sim \Omega_M^{0.55}$ (Carroll et al. 1992; Linder 2005), where $D(a)$ is the linear growth function as a function of scale factor a and Ω_M is the matter density relative to the critical density.
- (iii) Embed the survey into a larger volume, chosen such that the boundaries of this larger volume are sufficiently separated from the survey.
- (iv) Gaussian smooth the density field.
- (v) Generate a constrained Gaussian realization that

matches the observed density and interpolates over masked and unobserved regions (§2.3).

- (vi) Estimate the displacement field Ψ within the Zel’dovich approximation (§2.4).

(vii) Shift the galaxies by $-\Psi$. Since linear redshift-space distortions arise from the same velocity field, we shift the galaxies by an additional $-f(\Psi \cdot \hat{s})\hat{s}$ (where \hat{s} is the radial direction). In the limit of linear theory (i.e. large scales), this term exactly removes redshift-space distortions (Kaiser 1987; Hamilton 1998; Scoccimarro 2004). Denote these points by D .

- (viii) Construct a sample of points randomly distributed according to the angular and radial selection function and shift them by $-\Psi$. Note that we do not correct these for redshift-space distortions. Denote these points by S .

(ix) The reconstructed correlation function ξ is then given by the Landy-Szalay (Landy & Szalay 1993) estimator,

$$\xi = \frac{DD - 2DS + SS}{RR} \quad (1)$$

where DD etc are the number of pairs at a given separation between various sets of points. The random points R are distributed randomly according to the angular and radial selection functions; these are assumed to be different from those to generate S . We weight the points by an approximate minimum variance weight (Feldman et al. 1994),

$$w_i = \frac{1}{1 + \bar{n}(z_i)P(k_0)} \quad (2)$$

where \bar{n} is the redshift distribution at the galaxy redshift z_i and $P(k_0) = 40000(\text{Mpc}/h)^3$ is the power spectrum approximately at the BAO scale for SDSS LRGs.

2.3 Generating Constrained Realizations

Since the gravitational potential (and therefore, the displacement) depends non-locally on the matter overdensity, it is sensitive to regions of space either masked out by the survey or not surveyed at all. To handle this complication, we embed the survey into a larger region where the boundaries of this larger region are sufficiently far from the true survey (in what follows below, we pad by 200 Mpc/h). Since the density field on large scales can be approximated by a Gaussian density field, the problem of “filling” in the missing regions is then equivalent to the problem of generating constrained realizations of a Gaussian density field (Hoffman & Ribak 1991, see also Zaroubi et al. 1995, who demonstrate that the previous algorithm is equivalent to a Weiner filtering of the density field). Strictly speaking, one should marginalize over the ensemble of such realizations. However, as we demonstrate below, our results are insensitive to the details of this implementation. Therefore, for simplicity, we consider only a single realization.

We start by organizing the observed and constrained realization density fields into an N_{obs} element vector δ and an N_{embed} element vector $\tilde{\delta}$, related by the trivial projection \mathbf{P} on to the observed points, $\delta = \mathbf{P}\tilde{\delta}$. The Hoffman-Ribak algorithm is then

$$\tilde{\delta} = \tilde{\delta}_U + \tilde{\mathbf{C}}\mathbf{C}^{-1}(\delta - \mathbf{P}\tilde{\delta}_U) \quad (3)$$

where $\tilde{\delta}_U$ is an unconstrained Gaussian realization, with an assumed power spectrum $P(k)$. The covariance matrices \mathbf{C} and $\tilde{\mathbf{C}}$ are defined by the correlation function between pairs of pixels,

$$C_{ij} \equiv \langle \delta(\mathbf{r}_i)\delta(\mathbf{r}_j) \rangle, \quad (4)$$

where the correlation function is just the Fourier transform of the power spectrum. Note that \mathbf{C} is an $N_{\text{obs}} \times N_{\text{obs}}$ matrix and operates only on the observed pixels, while $\tilde{\mathbf{C}}$ has dimension $N_{\text{embed}} \times N_{\text{obs}}$ and relates the observations and constrained realization.

While this algorithm is straightforward in principle, a number of comments are in order regarding its implementation. The first concerns our choice of power spectrum for generating the constrained realization and covariance matrices. *Unlike* the algebraically similar problem of power spectrum estimation, we do have a measurement of the power

spectrum, which we use. A related issue is that in redshift space, the prior correlation function is not isotropic and translation-invariant. We ignore this subtlety for simplicity and use an isotropic correlation function. We demonstrate later that, for the SDSS DR7 geometry, the reconstructed correlation function is robust to these choices. Finally, we note that our prior power spectrum also includes a white noise component of amplitude \bar{n}^{-1} .

The second issue is computational. The dimensions of δ and $\tilde{\delta}$ are $N \sim \mathcal{O}(10^9)$, making direct manipulation impossible. To proceed, we use the fact that multiplication by \mathbf{C} is equivalent to a convolution by the correlation function (Padmanabhan et al. 2003). Since we have ignored the angular dependence of the power spectrum, we can implement this in $\mathcal{O}(N \log N)$ time using FFTs. The matrix inverse operations are implemented using a preconditioned conjugate gradient algorithm (Press et al. 1992) with the preconditioner being the convolution by the Fourier transform of $1/P(k)$. For an unmasked survey, this preconditioner is the exact inverse. The above allows us to generate constrained realizations in $\mathcal{O}(10)$ iterations.

2.4 Solving for the Displacement

To linear order, the displacement Ψ can be related to the density in redshift space by (Nusser & Davis 1994)

$$\nabla \cdot \mathbf{F} = \nabla \cdot \Psi + f\nabla \cdot (\Psi_s \hat{s}) = -\frac{\delta_{\text{gal}}}{b}, \quad (5)$$

where $\Psi_s \equiv \Psi \cdot \hat{s}$ is the displacement in the redshift direction and δ_{gal} is the galaxy overdensity. Assuming the Ψ is irrotational, we write $\Psi = \nabla\phi$ and solve for the scalar valued ϕ . The resulting equation resembles Poisson’s equation with an additional term for redshift-space distortions. However, the redshift-space term breaks the translational invariance of the problem and prevents us from solving this with FFTs¹. We solve this equation by converting all the derivatives to their finite difference counterparts and solve the resulting linear equation. We implement this using the parallel GMRES algorithm in the PETSC (Balay et al. 2011b,a, 1997) toolkit. Having computed ϕ , we obtain the displacement field by finite differences. An advantage of this formulation is that the algorithm is easily extended to non-Cartesian coordinate systems, although we do not use this feature in this work.

2.5 Fitting the Acoustic Feature

We briefly describe our fitting procedure below; a detailed description and tests of this procedure in in Paper II. We define a fiducial fitting model

$$\xi^{\text{fit}}(r) = B^2\xi_m(\alpha r) + A(r) \quad (6)$$

where

$$\xi_m(r) = \int \frac{k^2 dk}{2\pi^2} P_m(k) j_0(kr) e^{-k^2 a^2}, \quad (7)$$

and

$$A(r) = \frac{a_1}{r^2} + \frac{a_2}{r} + a_3. \quad (8)$$

¹ Note that in the plane-parallel approximation, translational invariance is restored.

Our template is determined by interpolating between the linear theory power spectrum and one with the BAO feature erased (Eisenstein et al. 2007b)

$$P_m(k) = [P_{\text{lin}}(k) - P_{\text{smooth}}(k)]e^{-k^2\Sigma_{\text{nl}}^2/2} + P_{\text{smooth}}(k). \quad (9)$$

For convenience, we choose to normalize this template to the observed correlation function at $r = 50 \text{ Mpc}/h$; this ensures $B^2 \sim 1$. The Σ_{nl} parameter smooths the BAO feature, modeling the degradation due to non-linear structure growth. The $e^{-k^2a^2}$ term is used to damp the oscillatory transform kernel $j_0(kr)$ at high- k to induce better numerical convergence in the integration. The $A(r)$ term, with the associated $a_{1,2,3}$ nuisance parameters, is used to help marginalize out the unmodeled broadband signal in the correlation function. This broadband signal includes redshift-space distortions, scale-dependent bias and any errors we make in our assumption of the model cosmology which might bias the acoustic peak.

Our distance constraints are captured by the scale dilation parameter α which represents the shift in the acoustic peak. An $\alpha > 1$ indicates a shift towards smaller scales and an $\alpha < 1$ indicates a shift towards larger scales.

We obtain the best-fit value of α by minimizing the χ^2 goodness-of-fit indicator

In order to compute the likelihood function $p(\alpha)$ given the measured correlation function, we start with

$$\chi^2(\alpha) = [\vec{d} - \vec{m}(\alpha)]^T C^{-1} [\vec{d} - \vec{m}(\alpha)] \quad (10)$$

where \vec{d} is the measured correlation function and $\vec{m}(\alpha)$ is the best-fit model at each α . We use a fiducial fitting range of $30\text{--}200h^{-1}\text{Mpc}$. C is a modified Gaussian covariance matrix described in detail in Paper II. We minimize this function for a grid of fixed values of α ; this step is exactly equivalent to marginalizing over the linear parameters a_i , and is a good approximation for the B^2 term as well. The likelihood distribution of α is then simply

$$p(\alpha_i) \propto e^{-\chi_i^2/2} \quad (11)$$

where χ_i is the χ^2 minimum at α_i and the proportionality constant is determined by ensuring that the probability integrates to one. In addition, we impose a 15% Gaussian prior on $\log(\alpha)$. While this prior does not affect the core of the probability distribution, it does suppress values of $\alpha \ll 1$ that correspond to the BAO scale being shifted to very large scales, reflecting our current state of knowledge about the background cosmology.

This probability distribution captures all the distance information of this data and is what we use when estimating cosmological parameters in Paper III. It is however convenient to summarize this information. We do so throughout this paper by reporting the mean $\langle\alpha\rangle$ and standard deviation σ_α for the data and each individual mock catalog, where $\sigma_\alpha^2 = \langle\alpha^2\rangle - \langle\alpha\rangle^2$ and

$$\langle\alpha^n\rangle = \int d\alpha p(\alpha)\alpha^n. \quad (12)$$

As we see below for the data and is discussed in greater detail in Paper II, $p(\alpha)$ is well approximated by a Gaussian and therefore completely characterized by the mean and standard deviation. It is also worth emphasizing that this procedure yields an independent measurement of the distance

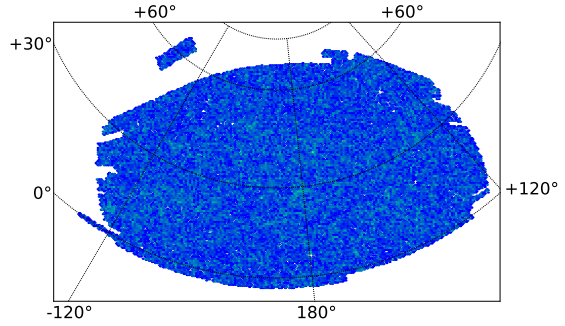


Figure 2. The footprint of the DR7 LRG sample used in this paper, plotted in equatorial coordinates and an Albers equal area projection. The area covered is 7189 deg^2 .

error for every mock, capturing the effects of sample fluctuations. Our analyses must therefore not just explore the distribution of α but also of σ_α as well (see below).

3 DATA AND SIMULATIONS

3.1 The LRG sample

The Sloan Digital Sky Survey (York et al. 2000) has imaged $\sim 10,000 \text{ deg}^2$ of the sky, and obtained spectra of nearly a million of the detected objects. The imaging was carried out by drift scanning the sky in photometric conditions (Hogg et al. 2001) in the *ugriz* bands (Fukugita et al. 1996; Smith et al. 2002) with the Apache Point 2.5m telescope (Gunn et al. 2006) using a specially designed wide field camera (Gunn et al. 1998). These data were processed by completely automated pipelines that detect and measure the photometric properties of the objects and astrometrically and photometrically calibrate these observations (Pier et al. 2003; Ivezić et al. 2004; Tucker et al. 2006; Padmanabhan et al. 2008). Subsamples from the resulting photometric samples were selected (Strauss et al. 2002; Eisenstein et al. 2001) for spectroscopy using a 640 fiber spectrograph. The SDSS has had three phases: SDSS-I and SDSS-II completed the observations described above in 2009 and the data were released in a series of seven data releases, with the SDSS Data Release 7 (Abazajian et al. 2009, DR7) being the final data release. The third phase of SDSS (Eisenstein et al. 2011, SDSS-III) started taking data in 2009 and includes the Baryon Oscillation Spectroscopic Survey (Schlegel et al. 2009, BOSS) as part of its science goals.

The sample that we consider for this analysis is the LRG sample. The motivation and selection of this sample is described in detail in Eisenstein et al. (2001) and we refer the interested reader to the description there. These galaxies are very luminous and therefore can probe cosmologically interesting volumes. Furthermore, they are generally old stellar systems with very uniform spectral energy distributions, characterized by a strong break at 4000\AA . This gives these galaxies a distinct color-flux-redshift relation, which allows them to be uniformly selected over a broad redshift range.

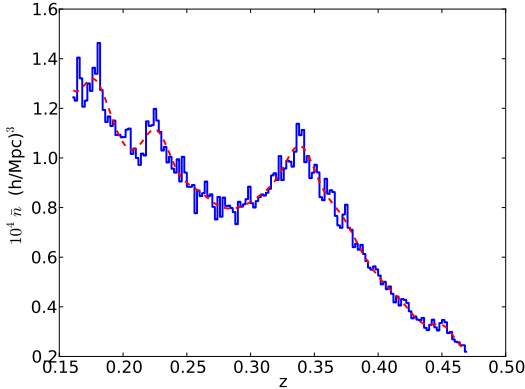


Figure 3. The redshift distribution of the DR7 LRG sample used in this paper. The dashed [red] line is a smooth fit to the redshift distribution used in the determination of the weights used in the correlation function.

The LRG samples have been used for a number of cosmological analyses in the SDSS, including the BAO detection in the SDSS (Eisenstein et al. 2005; Blake et al. 2007; Padmanabhan et al. 2007; Percival et al. 2007; Gaztañaga et al. 2009a,b; Kazin et al. 2010; Percival et al. 2010; Reid et al. 2010; Chuang & Wang 2011; Sawangwit et al. 2011). We use a sample identical to that used in Kazin et al. (2010) and refer the reader there for a detailed description of its construction.

Figure 2 shows the sky coverage of the sample that we consider. While the SDSS-II survey has data in both the Northern and Southern Galactic Caps, we focus on the contiguous footprint in the North, with a total area of 7189 deg². Figure 3 plots the number density of the LRG sample as function of redshift. We truncate the redshift distribution at $z = 0.16$, since the color selection of the LRG sample breaks down there. The redshift distribution is approximately constant out to a redshift of $z \sim 0.35$, falling off due to the magnitude limit of the sample beyond.

3.2 LasDamas Mock Galaxy Catalogs

We test our implementation of the reconstruction algorithm on mock galaxy catalogs created from the Large Suite of Dark Matter Simulations (LasDamas; McBride et al 2012, in prep). Our goals are (a) to demonstrate that reconstruction yields an unbiased and improved distance scale measurement, (b) to test the robustness of the reconstruction algorithm to its input parameters, and (c) to tune these parameters in a “blind” manner.

We use the publicly available mock galaxy catalogues constructed by the LasDamas collaboration², which are designed to simulate the SDSS LRG samples. We chose the gamma release of `lrgFull1` (in the LasDamas nomenclature) which best corresponds to our data sample. LasDamas assumes a flat Λ CDM cosmology, roughly consistent with WMAP5, with $\Omega_{\text{baryon}} = 0.04$, $\Omega_{\text{matter}} = 0.25$, $\Omega_{\Lambda} = 0.75$, $h = 0.7$, $n_s = 1.0$, and $\sigma_8 = 0.8$. The LRG mocks were

constructed from 40 “Oriana” N-body realizations, which were each run in a large cubical volume ($L = 2.4 h^{-1}$ Gpc) with 1280³ particles and initialized using second-order Lagrangian perturbation theory at $z = 49$. The mock galaxy catalogs were constructed by populating dark matter halos catalogs, where the halo occupation parameters were varied to match observed galaxy clustering measurements. The mock galaxy catalogs modeled the realism of observed data by modeling redshift distortions, matching the angular selection function of the SDSS DR7 LRG sample and spanning the redshift range of $z = 0.16 - 0.44$. We make one modification to the public catalogs to better match our analysis: we downsample the radial selection function to match our specific LRG data. This is necessary to properly model the galaxy numbers in the flux-limited region of the LRG selection at redshifts greater than $z = 0.36$. We make use of the catalogs covering only the northern galactic cap of the SDSS footprint (7214.34 sq.deg), which yield four mocks from each simulation for a total of 160 galaxy catalogs.

3.3 Fiducial Cosmologies

We conclude this section by discussing two technical details — our adopted definition of the sound horizon and the fiducial cosmology assumed in our analyses. We follow Eisenstein & Hu (1998) and assume the sound horizon specified by Eq.6 of that paper and defer a comparison of the different choices to Paper III. We use two fiducial cosmologies in our analyses below; while both of these are flat Λ CDM cosmologies, they differ in their choices of parameters. For the LasDamas simulations, we use the cosmology assumed for the simulations - a baryon density of $\Omega_b = 0.04$, a matter density of $\Omega_m = 0.25$, and a Hubble constant of 70 km/s/Mpc ($h = 0.7$). However, these choices differ significantly from the current best fit to the cosmic microwave background data from the WMAP satellite (Komatsu et al. 2011, hereafter WMAP7), with $\Omega_b = 0.0457$, $\Omega_m = 0.274$ and $h = 0.702$. In particular, the sound horizon assuming the WMAP7 cosmology is 152.76 Mpc, compared to 159.68 Mpc for the LasDamas cosmology, a difference larger than our claimed statistical accuracy. While, as we discuss below, an incorrect cosmology does not bias our distance scale, it does change the errors on the distance scale. This makes it important to iterate and choose a cosmology close to the best fit in the analysis. As we demonstrate below, the data are well fit by the WMAP7 cosmology and we use it as our fiducial model when analyzing the SDSS DR7 data.

4 RECONSTRUCTING SIMULATIONS

We start by discussing the impact of reconstruction on the LasDamas simulations. The top left panel is the unreconstructed real-space correlation function, with the BAO ring clearly visible and the correlation function independent of angle. Turning on redshift-space distortions destroys the isotropy of the correlation function, with the maximal distortion, as expected, parallel to the line of sight. The distortions at small r_{\perp} and $r_{\parallel} < 20\text{Mpc}/h$ are due to virial motions inside halos, so called “Fingers of God” (FoG). The bottom panels show the correlation functions after reconstruction, assuming a 15 Mpc/ h smoothing

² <http://lss.phy.vanderbilt.edu/lasdamas>

length to estimate the displacement field and the true values of the logarithmic growth rate f and the galaxy bias b . The most relevant feature for this paper is the enhanced BAO signal, apparent from the increased contrast of the BAO ring. Equally striking is the restored isotropy of the redshift-space correlation function, demonstrating that reconstruction is correcting for the large-scale redshift-space distortions. The breakdown on small scales is due to a combination of the fact that the model for the displacement field is based on linear theory and that reconstruction is imperfect on these scales. We also note that the fingers of God become more prominent, highlighting the tendency of reconstruction to blow up collapsed objects. It is important to emphasize that both these effects are restricted to small scales and have no effect of the acoustic scale.

We compress the 2D correlation functions by averaging over angle; the resulting correlation functions (both in real and redshift space) are in Figure 5. In both cases, we observe the BAO feature sharpened after reconstruction. In the case of the redshift-space distortions, the overall amplitude of the correlation function is also reduced due to the removal of linear redshift-space distortions. We find that the reconstructed redshift-space correlation function does not match its real-space counterpart on small scales, indicating that the linear theory correction is breaking down on these scales. However, the agreement on large ($r > 30\text{Mpc}/h$) scales is striking.

Figure 5 has a useful interpretation as a redistribution of pairs of galaxies across different scales. Recall that $r^2\xi$ is proportional to the number of excess pairs (over a random distribution) in an annulus of width dr centered at r . Since reconstruction does not change the total number of pairs but merely redistributes them over different scales, the area under these curves must be conserved. Comparing the correlation functions before and after reconstruction captures this redistribution of pairs. There are two effects worth noting, both of which are more easily noted in the real-space case. The first is a transferring of pairs from small scales ($r < 20\text{Mpc}/h$) to intermediate scales ($r \sim 50\text{Mpc}/h$), apparent in the fact that the unreconstructed correlation function is larger on small scales, with the trend reversed on intermediate scales. This is reconstruction reversing the infall of galaxies into overdensities. The second is that the unreconstructed correlation function is higher just before the BAO feature, due to pairs flowing out of the BAO feature. These flows are responsible for the smoothing of the BAO feature. The fact that the reconstructed correlation function is lower just before the BAO feature and then higher at the BAO peak is from the fact that reconstruction has moved these objects back into the BAO ring.

One metric to quantify the degree of reconstruction is to compare the values of Σ_{NL} (see Eq. 9) before and after reconstruction. While Σ_{NL} is poorly constrained in any single simulation, we can fit the average of the simulations before and after reconstruction. We find that Σ_{NL} decreases by close to 50% from 8.1 to 4.4 Mpc/h . This improvement is in line with theoretical estimates (Padmanabhan et al. 2009) and corresponds well with assumptions made for future surveys.

Figures 6 and 7 quantify the impact of reconstruction on the inferred distance α in real and redshift space respectively. Recall that α is the estimated distance relative to a

fiducial distance, which, in the case of the simulations, we choose to be the true comoving distance to the median redshift of the survey $z \sim 0.35$. Both the unreconstructed and reconstructed simulations yield unbiased distance estimates (i.e. $\langle \alpha \rangle = 1$) and the distances before and after reconstruction are clearly correlated with one another. Reconstruction, however, reduces the scatter in α from 3.0% to 2.0% in real space and from 3.3% to 2.1% in redshift space, an improvement of between a factor of 1.5 to 1.7. These figures also demonstrate that reconstruction noticeably reduces the number of outliers in the distance estimate, a direct effect of the increased significance of the BAO feature.

Before continuing, it is worth noting that the BAO scale in galaxies is expected to be biased at the $\sim 0.5\%$ level (or lower) (Padmanabhan & White 2009; Mehta et al. 2011). These biases are understood to arise from second-order terms in perturbation theory (Crocce & Scoccimarro 2008; Padmanabhan & White 2009) and are expected to be reduced by reconstruction (Padmanabhan et al. 2009; Noh et al. 2009; Mehta et al. 2011). However, the amplitude of these effects are much below what we can expect to observe with a single SDSS sized dataset and are expected to be only marginally detectable with the full ensemble of simulations. Table 1 verifies this expectation, demonstrating that any bias in the distance scale is less than 0.2%, much below our statistical precision. We therefore ignore these effects in all our subsequent analyses but note that they will become relevant as the statistical error decrease for future surveys.

The above distance accuracies are ensemble averages. Given the still relatively low significance of the detection of a BAO feature, statistical fluctuations may make the BAO feature more or less prominent. Since our fitting procedure marginalizes out smooth components in the correlation function, a less prominent BAO feature would result in a significantly degraded distance measurement. It is therefore interesting to quantify the effect of reconstruction not just on the ensemble distance accuracies, but also on the distance accuracy estimated for each individual simulation. Figures 8 and 9 summarize this information for real and redshift space respectively. The median errors agree well with the errors estimated from the ensemble distance measurements, confirming the validity of our error estimates. We also observe that, for the majority of the simulations ($\sim 98\%$), reconstruction reduces the distance error. For the remaining $\sim 2\%$, we find that the errors are very similar to those obtained before reconstruction. Furthermore, a number of these are cases where the distance scale itself is poorly measured. Paper II discusses these cases in more detail. Table 1 summarizes the above discussion, considering the recovered distances before and after reconstruction.

4.1 Robustness to Reconstruction Parameters

All of the above has assumed our default choices of parameters for reconstruction - a smoothing scale of 15 Mpc/h , the measured value of the galaxy bias ($b = 2.2$) and the input value of f . We also assume a concordance cosmology power spectrum in order to generate the constrained Gaussian realization. We explore the effects of varying these below. We use the simulations to determine the optimal smoothing scale and demonstrate that reconstruction is robust to variations in the other parameters.

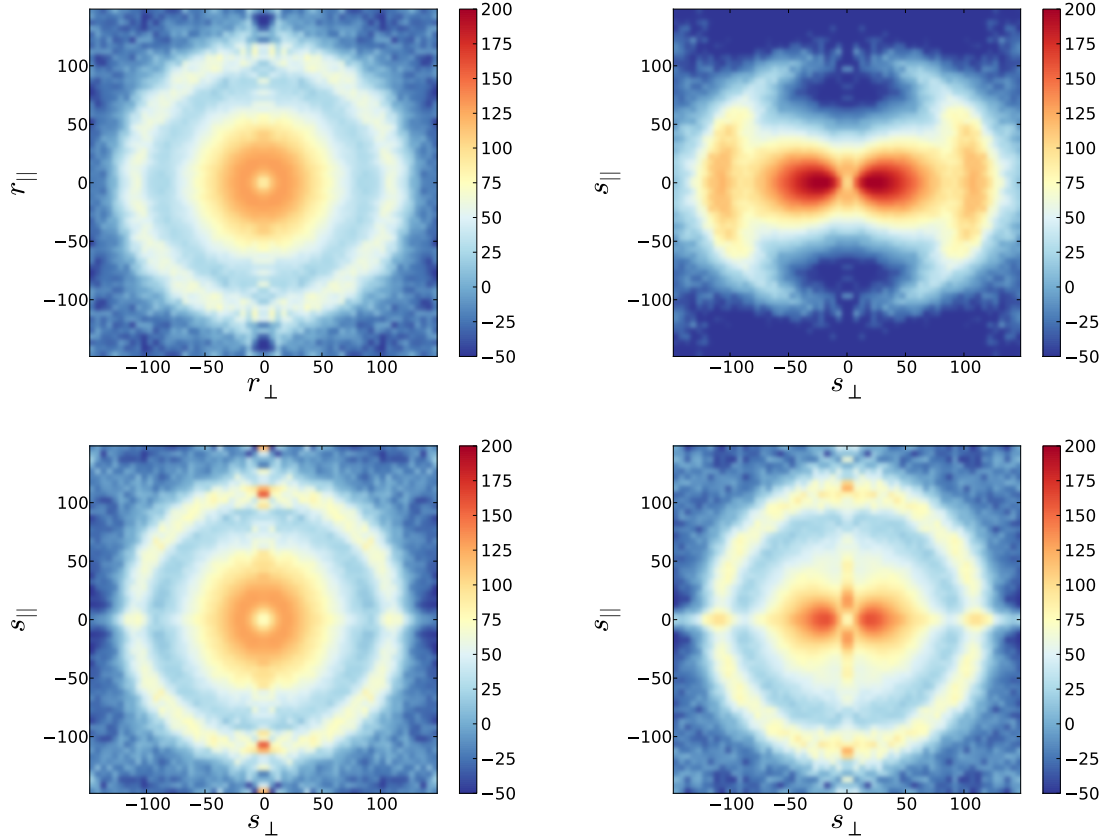


Figure 4. The LasDamas galaxy correlation function, averaged over the 160 simulations, as a function of the separation perpendicular (\perp) and parallel (\parallel) to the line of sight. The correlation functions have been scaled by r^2 to highlight the BAO feature. The top panels show the unreconstructed correlation functions, while the bottom panels show the reconstructed correlation functions; the left and right panels are real and redshift space respectively. The BAO feature is visible as a ring at $\sim 110 \text{Mpc}/h$ in the top left panel. Redshift space distortions destroy the isotropy of the correlation function (top right). Reconstruction both sharpens the BAO feature (highlighted in the bottom left panel) and restores the isotropy (bottom right) of the correlation function on the BAO scale.

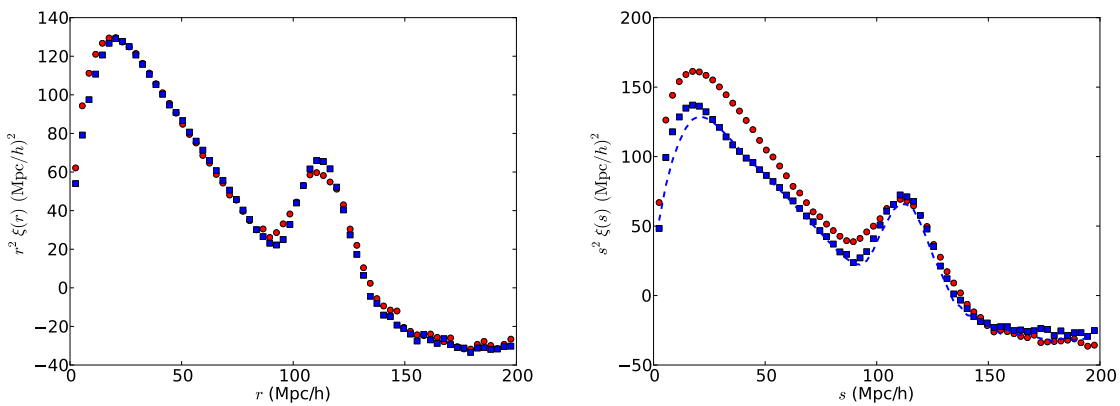


Figure 5. [left] The angle averaged correlation function in real space, before [red circles] and after [blue squares] reconstruction and averaging over the 160 LasDamas simulations. The reconstruction algorithm assumes the default parameters described in the text. The acoustic feature is clearly sharpened after reconstruction. [right] Same as the left panel, except in redshift space. Also shown for comparison is the average reconstructed real-space correlation [dashed line]. In addition to sharpening the acoustic feature, the reconstruction algorithm also reduces the effects of redshift-space distortions on the correlation function.

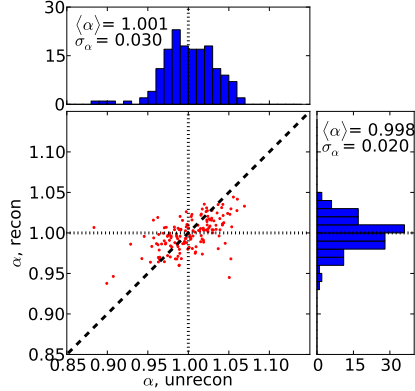


Figure 6. The distance scale, α estimated for the LasDamas simulations in real space, before (“unrecon”) and after (“recon”) reconstruction and their projected 1D distributions. The lines on the scatter plot mark the true ($\alpha = 1$) values as well as the equality ($\alpha_{\text{recon}} = \alpha_{\text{unrecon}}$) line. We find no evidence of a statistical bias in the recovered α values; reconstruction reduces the scatter in these values.

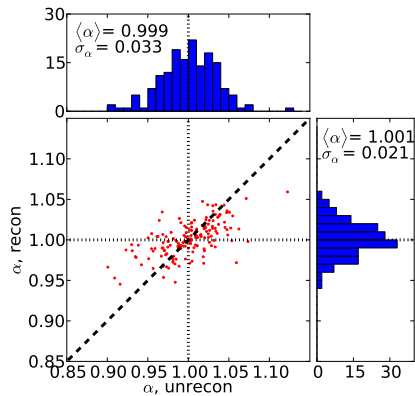


Figure 7. The same as Figure 6 except now in redshift space. The scatter in the recovered values is larger than the real-space case, with reconstruction still significantly reducing the scatter in these values.

Type	$\langle \alpha - 1 \rangle$	σ_α	$\widetilde{\sigma}_\alpha$	$n(\sigma_\alpha > 0.07)$
Real, unrecon	0.1	3.0	3.1	5
Real, recon	-0.2	2.0	2.2	0
Redshift, unrecon	-0.1	3.3	3.3	8
Redshift, recon	0.1	2.1	2.3	0

Table 1. A summary of the effect of reconstruction on the distance estimates, in real and redshift space. The $\langle \alpha - 1 \rangle$ and σ_α numbers are in percent. For all these cases, we reconstruct using our default choices of parameters. The second column is the bias in the distance in percent. The third column is the error in the distance estimated from the ensemble of the LasDamas simulations, while the fourth column is the median of the errors estimated per simulation, with the agreement between the two testing our error estimates. The last column shows the number of cases where the error in the distance is greater than 7%. In all of these metrics, reconstruction improves the precision of the distance estimates.

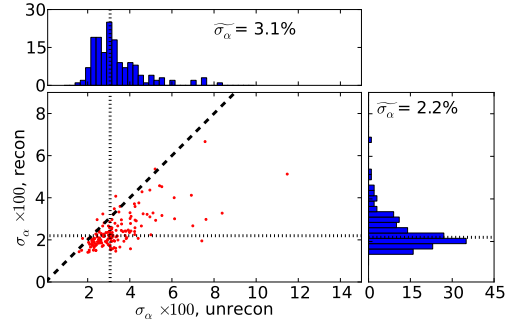


Figure 8. The error on the distance scale before and after reconstruction, as individually estimated for each LasDamas simulation in real space. The short dashed line has slope 1; the fact that most points lie below the line demonstrates the efficacy of reconstruction. The horizontal and vertical lines mark the median error before and after reconstruction. Note also the large scatter in the estimated errors, due to the still relatively low significance of the BAO detection in the DR7 survey volume.

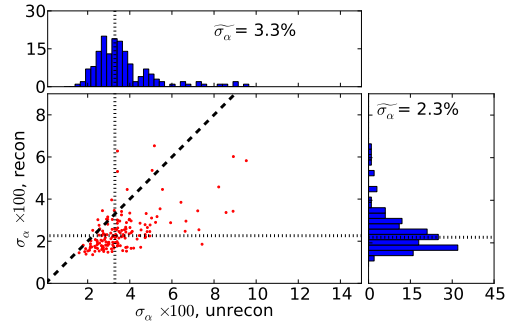


Figure 9. The same as Figure 8 except in redshift space.

The most important of the reconstruction parameters is the scale used to smooth the density field before estimating the potential. For scales too small, the fidelity of the potential reconstruction is affected by noise from the finite numbers of galaxies. At the other extreme, over-smoothing reduces the estimated displacements (an infinite smoothing scale leaves the galaxies at their original positions) and reduces the effectiveness of reconstruction. In the limit of a high number density of galaxies, the above argument suggests choosing a smoothing scale as small as possible; however, as argued in Eisenstein et al. (2007b), the bulk of the smoothing comes from scales between $k = 0.02$ to 0.2 h/Mpc , suggesting that one reaches diminishing returns for scales smaller than ~ 5 Mpc/h . The number density of the LRG sample is $\leq 10^{-4} h^3/\text{Mpc}^3$, which implies that the shot noise power spectrum crosses at a scale of $\sim 0.15 h/\text{Mpc}$, suggesting smoothing on scales larger than $\sim 10 \text{Mpc}/h$.

Figure 10 plots the reconstructed 2D correlation functions for different choices of the smoothing scale. For large

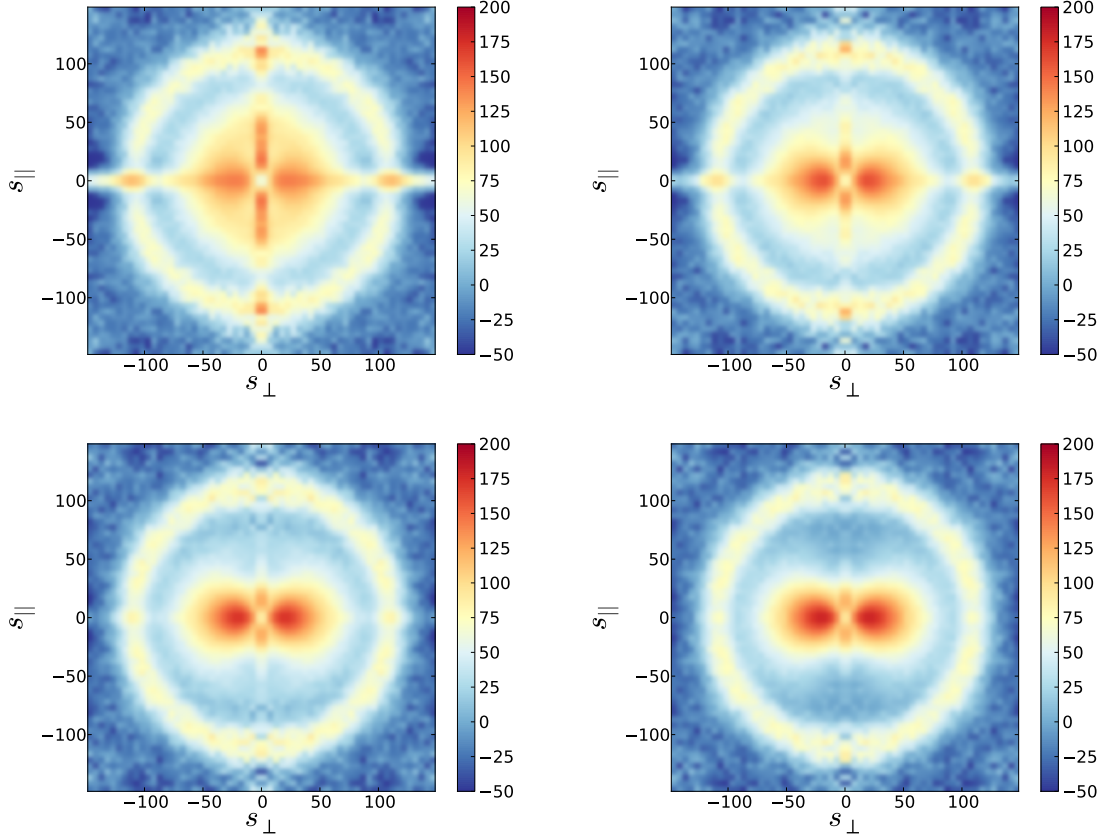


Figure 10. The impact of changing the smoothing length on reconstruction for the 2D correlation functions. The panels correspond to smoothing scales of 10 (top left), 15 (top right), 20 (bottom left) and 25 (bottom right) Mpc/h. Note the prominent distortions in the correlation function at small scales for the 10 Mpc/h smoothing scale and the degraded reconstruction for the 25 Mpc/h case. Our fiducial choice is the 15 Mpc/h case.

Smoothing	$\langle \alpha - 1 \rangle$	σ_α	$\tilde{\sigma}_\alpha$	$n(\sigma_\alpha > 0.07)$
15 Mpc/h	0.1	2.1	2.3	0
20 Mpc/h	0.4	2.3	2.5	0
25 Mpc/h	0.6	2.6	2.6	0

Table 2. Analogous to Table 1, except as a function of the smoothing scale input to the redshift-space reconstruction. As before, the $\langle \alpha - 1 \rangle$ and σ_α numbers are in percent. In all cases, the distance is unbiased, but as expected, we find the error increasing as a function of the smoothing scale. Reconstruction after smoothing at 10 Mpc/h distorts the shape of the correlation function and our model is no longer a good fit to the shape. We use 15 Mpc/h as our fiducial smoothing scale.

smoothing scales, the degree of reconstruction is clearly degraded, although even in these cases, the BAO feature is still enhanced relative to the case of no reconstruction. This emphasizes the fact that it is large-scale flows that are responsible for the erasure of the BAO feature; even a large smoothing scale can effectively reverse these. At the other extreme at 10 Mpc/h, we find that reconstruction can strongly distort the correlation function on small scales. A useful picture to understand the distortions at small perpendicular separation is to remember that reconstruction effectively repels close pairs of particles. Since the smoothing scale aver-

ages the shot noise in the input density field, insufficiently smoothing the field pushes apart noise fluctuations with an additional enhancement in the line of sight direction (generating its own Fingers of God).

The second feature is the excess at $r_{||} = 0$. An examination of Figure 4 shows that traces of this feature exist in the real-space correlation function as well. Unlike the redshift-space case, the reconstruction procedure in real space does not have a preferred direction. This feature can be traced back to our definition of the radial selection function. Since we do not know the mean density of the galaxies as a function of redshift, we simply define it by randomly resampling the observed galaxy redshifts. This suppresses radial density fluctuations and can create features in the transverse direction. As before, increasing the smoothing scale reduces both of these.

Figure 11 plots the angle averaged correlation function. We find that the correlation function is strongly distorted on small scales for the 10 Mpc/h smoothing scale; increasing the smoothing scales removes these distortions. Given our desire to choose the smallest smoothing scale possible, we adopt 15 Mpc/h as our fiducial choice. Table 2 summarizes the distance constraints as a function of smoothing scale and shows the same trends discussed above.

While the smoothing scale is the most important parameter input to the reconstruction algorithm, there are a

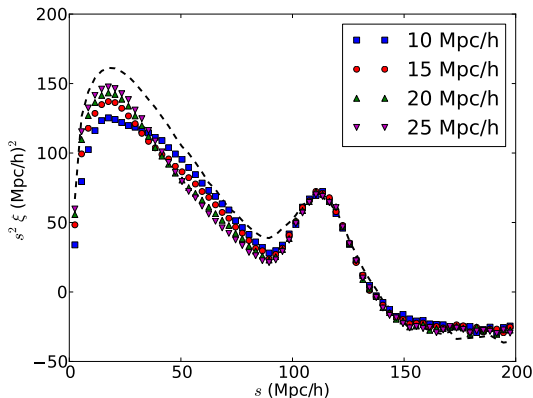


Figure 11. The averaged reconstructed correlation functions in redshift space for the LasDamas simulations, as a function of the reconstruction smoothing scale. Also plotted for reference [dashed line] is the unreconstructed correlation function. Our fiducial smoothing length is 15 Mpc/h.

number of other inputs - the galaxy bias b , the logarithmic growth rate of structure f , and the power spectrum used for the constrained realizations. The galaxy bias and the input power spectrum are constrained by measurements of the unreconstructed correlation function, while $f \sim \Omega_M^{0.55}$ can be constrained by CMB measurements. While we adopt these fiducial values for our measurements, an immediate question is how sensitive reconstruction is to these choices. Table 3 summarizes the impact of changing these values. We vary the bias and f by $\pm 20\%$ and we consider two different choices for a fiducial power spectrum - a power spectrum with the BAO features erased (Eisenstein & Hu 1998) and a constant $P(k) = 10^4 (\text{Mpc}/h)^3$. Of these, the bias has the strongest effect on reconstruction. An overestimate of the bias results in an underestimate of the density field, reducing the derived displacement field. On the other hand, underestimates of the bias result in an overestimate of the density field and over-corrects the displacements. While the distance scale obtained is still unbiased, Table 3 demonstrates including the uncertainty in the galaxy bias in reconstruction would increase the statistical uncertainty of the measurement. However, as Table 3 also shows, even for large variations in the bias (recall that a 20% uncertainty in the bias corresponds to a 40% uncertainty in the normalization of the correlation function, much larger than most estimates of the bias), this additional scatter is subdominant to our errors. We also observe the impact of mis-estimating the bias on the inferred error in the mocks is much less than our quoted statistical errors.

One of the most prominent effects of reconstruction was the restoration of the isotropy of the correlation function. Since this depends on the choice of f , an immediate question is how sensitive reconstruction is to the particular choice. Figure 12 plots the 2D correlation function with $f = 0$. This turns off both the modifications to the continuity equation in redshift space, as well as the additional line of sight displacements that correct for the redshift-space distortions. We find that the BAO feature is still improved, although the correlation function is still strongly distorted from isotropy. Less drastic variations in the value of f (although larger than our

Case	$\sigma(\Delta\alpha)$	r	$\sigma(\Delta\sigma_\alpha)$	r
$b=1.8$ (-20%)	0.9	0.92	0.3	0.94
$b=2.6$ (+20%)	0.6	0.97	0.2	0.97
$f=0.5$ (-20%)	0.2	1.00	0.1	1.00
$f=0.8$ (+20%)	0.2	1.00	0.1	1.00
Pk, no-wiggle	0.0	1.00	0.0	1.00
Pk, shot-noise	0.3	0.99	0.1	0.99

Table 3. The impact of changing the values of the galaxy bias, f and the input power spectrum for the constrained Gaussian from their fiducial values. For each mock, we compute the difference in distance, $\Delta\alpha$ and error, $\Delta\sigma_\alpha$ from the fiducial choice of parameters. We report both the scatter in these quantities (in percent) as well as the cross correlation r with the fiducial case. In all cases, we see that changing these parameters yields distances and errors that are almost perfectly correlated with those obtained using our fiducial parameters. The largest effect is seen for the galaxy bias which directly controls the displacement field.

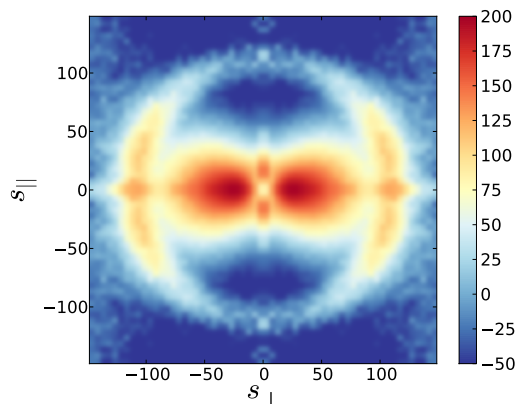


Figure 12. The 2D reconstructed correlation function, but without the redshift-space distortion corrections (i.e. setting $f = 0$ in the reconstruction algorithm). While the BAO feature is more prominent, redshift-space distortion still strongly distorts the BAO feature.

current errors on Ω_m) are in Table 3. Even more strongly than in the case of the bias, we find that this additional error is much smaller than our statistical error, demonstrating the robustness of reconstruction.

Finally, we consider varying the inputs to the constrained realizations. We consider two alternative power spectra - one with the BAO feature erased and the other with no clustering signal - and we find that reconstruction is robust to these choices as well. These results are dependent on the geometry of the survey and could possibly change for different geometries.

5 RECONSTRUCTING DATA

We now apply reconstruction to the DR7 data set. Our fiducial choice of parameters is a 15 Mpc/h smoothing length, a galaxy bias of 2.2 and the WMAP7 cosmology. Figure 13 plots the angle averaged DR7 correlation function before and after reconstruction. We find that reconstruction on the DR7 data demonstrates the same features seen in the

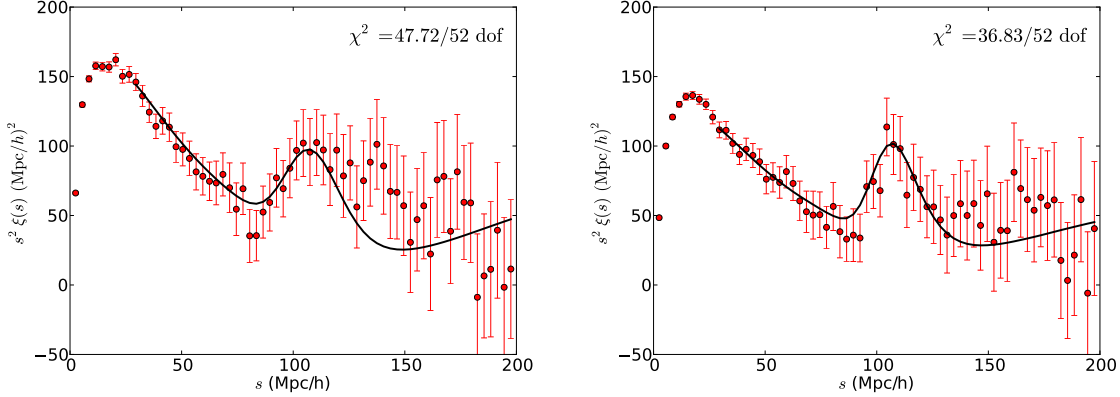


Figure 13. The unreconstructed [left] and reconstructed [right] DR7 angle averaged correlation function. The error bars are the standard deviation of the 160 LasDamas simulations. These errors are however highly correlated from bin to bin and therefore no conclusions as to significance should be drawn from these figures. The solid line is the best fit model to these data. As in the simulations, the acoustic feature appears sharpened.

LasDamas simulations. The amplitude of the intermediate-scale correlation function decreases due to the correction of redshift-space distortions, while the transition into the BAO feature at $\sim 80 - 100$ Mpc/h is sharpened.

The correlated nature of the errors makes it difficult to quantitatively assess the impact of reconstruction on these data. Figure 14 plots the χ^2 surface for α both before and after reconstruction. We note that the χ^2 minimum after reconstruction is visibly narrower, indicating an improvement in the distance constraints. This improvement is also summarized in the first two lines of Table 4 which shows that reconstruction reduces the distance error from 3.5% to 1.9%. These distance constraints are also consistent with the errors estimated from the LasDamas simulations.

Figure 14 also plots the χ^2 surface for a template without a BAO feature, using the “no-wiggle” form of Eisenstein & Hu (1998). The lack of a well defined minimum either before or after reconstruction indicates that our distance constraints are indeed coming from the presence of a BAO feature and not any broad band features in the correlation function. The difference in χ^2 between the templates with and without a BAO feature also provides an estimate of the significance of the BAO detection in these data. Reconstruction improves this detection significance from 3.3σ (consistent with previous measurements) to 4.2σ . This is not the only measure of the detection significance possible; Paper II discusses these in more detail.

As before, we would like to demonstrate the robustness of the results to the various parameters of the reconstruction algorithm. Table 4 lists the recovered distances varying the smoothing scale, input bias, growth rate (f), and prior power spectrum; for each of these cases, we recover distances consistent with the fiducial choices of parameters.

Our final test is the impact of the assumed fiducial cosmology. We consider two cases in Table 4: flat Λ CDM cosmologies with $\Omega_M = 0.2$ and 0.35 . In both of these cases, we adjust the Hubble constant and the baryon density Ω_b to keep the physical densities $\Omega_b h^2$ and $\Omega_M h^2$ equal to their WMAP7 values. This prescription leaves the CMB unchanged, but alters the distance-redshift relation. We find that the estimated values of α are significantly different from

the fiducial case. However, note that the physical observable is not α , but $D_V/r_s = \alpha(D_V/r_s)_{\text{fid}}$. Comparing this across the three cosmologies (second column, Table 4), we find it insensitive to the choice of cosmology.

The distance information from these BAO measurements may be summarized into a probability distribution $p(D_V/r_s)$, plotted in Figure 15 and summarized in the second column of Table 4. Unlike α , these measurements no longer make reference to a fiducial cosmology. One may however freely convert between $p(\alpha)$ and $p(D_V/r_s)$ by multiplying the latter by $(D_V/r_s)_{\text{fid}}$. We use the results in Figure 15 to explore the cosmological consequences of these measurements in Paper III. If we assume a perfectly measured sound horizon, these measurements can be converted into a distance measurement in Gpc. Using a sound horizon of 152.76 Mpc, we get a distance to $z = 0.35$ of 1.356 ± 0.025 Gpc. Note that these numbers do not have h^{-1} factors in them. Of course, the sound horizon is not perfectly measured and its uncertainty must be taken into account when fitting for cosmologies. Paper III discusses the methodologies and results in detail.

6 DISCUSSION

We present the results of the density field reconstruction on the BAO feature on the SDSS DR7 LRG data. This is the *first* application of reconstruction on a galaxy redshift survey, resulting in a 1.8 factor reduction in the distance error to a $z = 0.35$, equivalent to a *tripling* of the survey volume. This is the first in a series of three papers; Paper II describes the fitting of the correlation function, while Paper III explores the cosmological implications of these results.

Our principal results and conclusions are :

- (i) We modify the Eisenstein et al. (2007a) reconstruction algorithm to account for the effects of survey boundaries and redshift-space distortions and test it on the mock catalogs from the LasDamas suite of simulations. These mock catalogs have been designed to both match the SDSS survey geometry as well as the redshift distribution and clustering properties of the SDSS LRG sample.

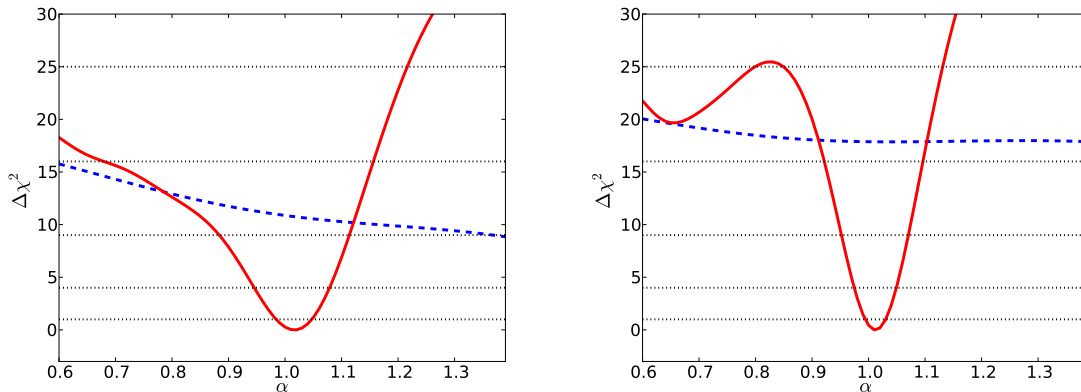


Figure 14. The $\Delta\chi^2$ surface as a function of α before [left] and after [right] reconstruction. The solid [red] line uses our default template with a BAO feature in the correlation function, while the dashed [blue] line uses the “no-wiggle” form of Eisenstein & Hu (1998). Reconstruction narrows the χ^2 minimum, reflecting the improved distance constraints. The difference between the solid and dashed lines estimates the significance of the detection of the BAO feature; the horizontal dotted lines mark the 1 to 5 σ significance level. Reconstruction increases the detection significance from 3.3 to 4.2 σ .

Case	$\alpha - 1 (\times 100)$	D_V/r_s	D_V (Gpc)
Unrecon	1.3 ± 3.5	8.89 ± 0.31	1.358 ± 0.047
Recon	1.2 ± 1.9	8.88 ± 0.17	1.356 ± 0.025
Smoothing, 20 Mpc/h	0.9 ± 2.1	8.85 ± 0.18	1.352 ± 0.028
b=1.8 (-20%)	1.4 ± 2.0	8.89 ± 0.18	1.358 ± 0.027
b=2.6 (+20%)	1.4 ± 1.9	8.89 ± 0.16	1.359 ± 0.025
f=0.5 (-20%)	1.1 ± 1.9	8.87 ± 0.16	1.355 ± 0.025
f=0.8 (+20%)	1.5 ± 1.9	8.90 ± 0.16	1.360 ± 0.025
Pk, no-wiggle	1.2 ± 1.9	8.88 ± 0.17	1.356 ± 0.025
Pk, shot-noise	1.5 ± 1.9	8.90 ± 0.17	1.360 ± 0.026
$\Omega_M = 0.20$	15.9 ± 2.4	8.93 ± 0.18	1.377 ± 0.028
$\Omega_M = 0.35$	-7.6 ± 1.8	8.93 ± 0.17	1.378 ± 0.026

Table 4. The comoving distance to $z = 0.35$, expressed (i) as $\alpha \equiv D_V/r_s/(D_V/r_s)_{\text{fid}}$ (ii) D_V/r_s and (iii) D_V assuming the fiducial value of r_s (and ignoring errors). The first group of numbers compares the unreconstructed and reconstructed cases (assuming our default reconstruction parameters). The distances obtained are consistent, but reconstruction reduces the error by a factor of 1.8, resulting in a distance precise to 1.9%. The second group explores the impact of changing the various reconstruction parameters (as in Tables 2 and 3; both the distance and its error are robust to any of these changes). Finally, we consider changing the fiducial cosmology (keeping the physical densities fixed). In this case, we expect α to change, since our fiducial distance changes, but the derived distances (both absolute and relative to the sound horizon) are unchanged. Note that the errors do change, reflecting changes in the volume relative to the acoustic scale.

(ii) We find that reconstruction both sharpens the BAO feature and restores the isotropy of the correlation function on large scales. The nonlinear smoothing of the BAO feature decreases from 8.1 to 4.4 Mpc/h, in line with theoretical estimates (Padmanabhan et al. 2009).

(iii) We find that reconstruction improves the distance estimates, reducing the median error of the LasDamas simulations from 3.3% to 2.3%. Furthermore, reconstruction also significantly reduces the number of outliers as a result of improving the detectability of the BAO feature.

(iv) We calibrate the smoothing scale input to the reconstruction algorithm and find that the optimal scale lies between ~ 15 to 20 Mpc/h; we adopt 15 Mpc/h as our fiducial value. Choosing too small a smoothing scale results in prominent artifacts in the correlation function, while too large a scale degrades the efficacy of reconstruction.

(v) We demonstrate the reconstruction is robust to the

choices of galaxy bias b , the rate of growth of structure f and the fiducial power spectrum used to interpolate missing data and pad the survey edges.

(vi) Applying reconstruction to the SDSS DR7 LRG data, we measure a relative distance to $z = 0.35$ of $D_V/r_s = 8.88 \pm 0.17$, compared with 8.89 ± 0.31 before reconstruction. The two distances are consistent, but reconstruction reduced the error from 3.5% to 1.9%, a factor of 1.8, equivalent to tripling the survey volume.

(vii) Reconstruction also improves the detectability of a BAO feature (relative to a model with feature erased) from 3.3σ to 4.2σ .

We can compare our results to the results of Percival et al. (2010) and Kazin et al. (2010), who analyzed similar samples with different (albeit related) fitting methodologies. Percival et al. (2010) analyze a combination of the

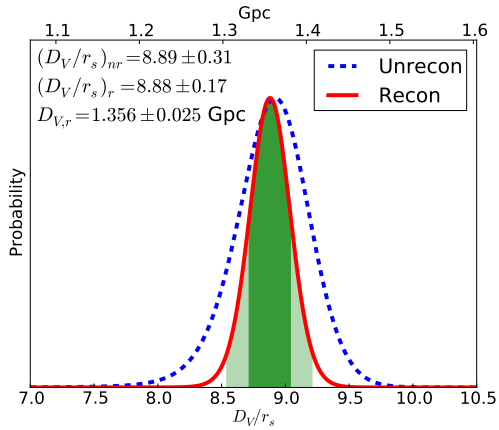


Figure 15. The probability of α before [blue, dashed] and after [red, solid] reconstruction. The mean and standard deviations of the two distributions is also listed. The shaded regions show the 1σ [dark shaded] and 2σ [light shaded] regions of the reconstructed probability distribution.

SDSS LRG data as well as lower redshift data from the SDSS Main galaxy sample. Their primary distance constraints are therefore reported at a lower redshift from ours: $D_V/r_s(z = 0.275) = 7.19 \pm 0.19$, a 2.7% measurement. Comparing these results with ours requires assuming a model to transform to a higher redshift. This comparison is done in detail in Paper III. We can however scale our results to this redshift (assuming that α does not change significantly with redshift) to obtain 7.15 ± 0.13 . These results are also consistent with Kazin et al. (2010) who obtain 7.17 ± 0.25 . We note that our error before reconstruction is larger than the Percival et al. (2010) results; this is however expected given the somewhat larger volume of that sample. Percival et al. (2010) also split their sample into two redshift slices with their higher redshift slice correspond to our measurements. They obtain $D_V/r_s(z = 0.35) = 9.11 \pm 0.30$, consistent with our results before reconstruction.

Our results have important implications for current and future surveys. All of these surveys have assumed some level of reconstruction for their projected constraints. This work retires a major risk for these surveys, being the first application to data. Furthermore, the degree of reconstruction assumed (a reduction of the nonlinear smoothing scale by 50%) is consistent with what this work has achieved.

This work has also limited itself to the angle averaged correlation function. One of the promises of the BAO method is the ability to measure both the angular diameter distance and the Hubble constant. These measurements are complicated by the loss of isotropy in the correlation function due to redshift-space distortions. As this paper has shown, reconstruction has the potential to undo the effects of redshift-space distortions and could significantly improve measurements of the anisotropic BAO signal. We will explore this in future work.

This paper has demonstrated that reconstruction is feasible on data and that it can significantly improve the distance constraints. We expect that reconstruction will become a standard method for analyzing the BAO signal from large redshift surveys.

Funding for the Sloan Digital Sky Survey (SDSS) and

SDSS-II has been provided by the Alfred P. Sloan Foundation, the Participating Institutions, the National Science Foundation, the U.S. Department of Energy, the National Aeronautics and Space Administration, the Japanese Monbukagakusho, and the Max Planck Society, and the Higher Education Funding Council for England. The SDSS Web site is <http://www.sdss.org/>.

The SDSS is managed by the Astrophysical Research Consortium (ARC) for the Participating Institutions. The Participating Institutions are the American Museum of Natural History, Astrophysical Institute Potsdam, University of Basel, University of Cambridge, Case Western Reserve University, The University of Chicago, Drexel University, Fermilab, the Institute for Advanced Study, the Japan Participation Group, The Johns Hopkins University, the Joint Institute for Nuclear Astrophysics, the Kavli Institute for Particle Astrophysics and Cosmology, the Korean Scientist Group, the Chinese Academy of Sciences (LAMOST), Los Alamos National Laboratory, the Max-Planck-Institute for Astronomy (MPIA), the Max-Planck-Institute for Astrophysics (MPA), New Mexico State University, Ohio State University, University of Pittsburgh, University of Portsmouth, Princeton University, the United States Naval Observatory and the University of Washington.

We thank the LasDamas collaboration for making their galaxy mock catalogs public. We thank Cameron McBride for assistance in using the LasDamas mocks and comments on earlier versions of this work. We thank Martin White for useful conversations on reconstruction. NP and AJC are partially supported by NASA grant NNX11AF43G. DJE, XX, and KM were supported by NSF grant AST-070725 and NASA grant NNX07AH11G. This work was supported in part by the facilities and staff of the Yale University Faculty of Arts and Sciences High Performance Computing Center.

REFERENCES

- Abazajian K. N. et al., 2009, *ApJS*, 182, 543
 Angulo R. E., Baugh C. M., Frenk C. S., Lacey C. G., 2008, *MNRAS*, 383, 755
 Balay S. et al., 2011a, PETSc users manual. Tech. Rep. ANL-95/11 - Revision 3.2, Argonne National Laboratory
 Balay S. et al., 2011b, PETSc Web page. [Http://www.mcs.anl.gov/petsc](http://www.mcs.anl.gov/petsc)
 Balay S., Gropp W. D., McInnes L. C., Smith B. F., 1997, in *Modern Software Tools in Scientific Computing*, Arge E., Bruaset A. M., Langtangen H. P., eds., Birkhäuser Press, pp. 163–202
 Beutler F. et al., 2011, *MNRAS*, 416, 3017
 Blake C., Collister A., Bridle S., Lahav O., 2007, *MNRAS*, 374, 1527
 Blake C. et al., 2011a, *MNRAS*, 415, 2892
 Blake C., Glazebrook K., 2003, *ApJ*, 594, 665
 Blake C. et al., 2011b, *ArXiv e-prints*
 Blake C. et al., 2011c, *MNRAS*, 1598
 Bond J. R., Efstathiou G., 1984, *ApJ*, 285, L45
 Bond J. R., Efstathiou G., 1987, *MNRAS*, 226, 655
 Carroll S. M., Press W. H., Turner E. L., 1992, *ARA&A*, 30, 499
 Chuang C.-H., Wang Y., 2011, *ArXiv e-prints*
 Cole S. et al., 2005, *MNRAS*, 362, 505

- Crocce M., Scoccimarro R., 2008, *Phys. Rev. D*, 77, 023533
- Drinkwater M. J. et al., 2010, *MNRAS*, 401, 1429
- Efstathiou G., Bond J. R., 1999, *MNRAS*, 304, 75
- Eisenstein D. J. et al., 2001, *AJ*, 122, 2267
- Eisenstein D. J., Hu W., 1998, *ApJ*, 496, 605
- Eisenstein D. J., Hu W., Tegmark M., 1998, *ApJ*, 504, L57
- Eisenstein D. J., Seo H.-J., Sirko E., Spergel D. N., 2007a, *ApJ*, 664, 675
- Eisenstein D. J., Seo H.-J., White M., 2007b, *ApJ*, 664, 660
- Eisenstein D. J. et al., 2011, *AJ*, 142, 72
- Eisenstein D. J. et al., 2005, *ApJ*, 633, 560
- Feldman H. A., Kaiser N., Peacock J. A., 1994, *ApJ*, 426, 23
- Fukugita M., Ichikawa T., Gunn J. E., Doi M., Shimasaku K., Schneider D. P., 1996, *AJ*, 111, 1748
- Gaztañaga E., Cabré A., Castander F., Crocce M., Fosalba P., 2009a, *MNRAS*, 399, 801
- Gaztañaga E., Cabré A., Hui L., 2009b, *MNRAS*, 399, 1663
- Goldberg D. M., Strauss M. A., 1998, *ApJ*, 495, 29
- Gunn J. E. et al., 1998, *AJ*, 116, 3040
- Gunn J. E. et al., 2006, *AJ*, 131, 2332
- Guzik J., Bernstein G., Smith R. E., 2007, *MNRAS*, 375, 1329
- Hamilton A. J. S., 1998, in *Astrophysics and Space Science Library*, Vol. 231, *The Evolving Universe*, D. Hamilton, ed., p. 185
- Hill G. J. et al., 2008, in *Astronomical Society of the Pacific Conference Series*, Vol. 399, *Panoramic Views of Galaxy Formation and Evolution*, T. Kodama, T. Yamada, & K. Aoki, ed., p. 115
- Ho S. et al., 2012, *ArXiv e-prints*
- Hoffman Y., Ribak E., 1991, *ApJ*, 380, L5
- Hogg D. W., Finkbeiner D. P., Schlegel D. J., Gunn J. E., 2001, *AJ*, 122, 2129
- Hu W., Haiman Z., 2003, *Phys. Rev. D*, 68, 063004
- Hu W., Sugiyama N., 1996, *ApJ*, 471, 542
- Hu W., Sugiyama N., Silk J., 1997, *Nature*, 386, 37
- Huff E., Schulz A. E., White M., Schlegel D. J., Warren M. S., 2007, *Astroparticle Physics*, 26, 351
- Ivezić Ž. et al., 2004, *Astronomische Nachrichten*, 325, 583
- Jeong D., Komatsu E., 2006, *ApJ*, 651, 619
- Kaiser N., 1987, *MNRAS*, 227, 1
- Kazin E. A. et al., 2010, *ApJ*, 710, 1444
- Komatsu E. et al., 2011, *ApJS*, 192, 18
- Landy S. D., Szalay A. S., 1993, *ApJ*, 412, 64
- Laureijs R. et al., 2011, *ArXiv e-prints*
- Linder E. V., 2003, *Phys. Rev. D*, 68, 083504
- Linder E. V., 2005, *Phys. Rev. D*, 72, 043529
- Matsubara T., 2008a, *Phys. Rev. D*, 78, 083519
- Matsubara T., 2008b, *Phys. Rev. D*, 77, 063530
- Mehta K., Cuesta A. J., Xu X., Eisenstein D. J., Padmanabhan N., 2012, *MNRAS*, submitted
- Mehta K. T., Seo H.-J., Eckel J., Eisenstein D. J., Metchnik M., Pinto P., Xu X., 2011, *ApJ*, 734, 94
- Meiksin A., White M., Peacock J. A., 1999, *MNRAS*, 304, 851
- Noh Y., White M., Padmanabhan N., 2009, *Phys. Rev. D*, 80, 123501
- Nusser A., Davis M., 1994, *ApJ*, 421, L1
- Padmanabhan N. et al., 2008, *ApJ*, 674, 1217
- Padmanabhan N. et al., 2007, *MNRAS*, 378, 852
- Padmanabhan N., Seljak U., Pen U. L., 2003, *New Ast.*, 8, 581
- Padmanabhan N., White M., 2009, *Phys. Rev. D*, 80, 063508
- Padmanabhan N., White M., Cohn J. D., 2009, *Phys. Rev. D*, 79, 063523
- Peebles P. J. E., Yu J. T., 1970, *ApJ*, 162, 815
- Percival W. J., Cole S., Eisenstein D. J., Nichol R. C., Peacock J. A., Pope A. C., Szalay A. S., 2007, *MNRAS*, 381, 1053
- Percival W. J. et al., 2010, *MNRAS*, 401, 2148
- Pier J. R., Munn J. A., Hindsley R. B., Hennessy G. S., Kent S. M., Lupton R. H., Ivezić Ž., 2003, *AJ*, 125, 1559
- Press W. H., Teukolsky S. A., Vetterling W. T., Flannery B. P., 1992, *Numerical recipes in C. The art of scientific computing*, Press, W. H., Teukolsky, S. A., Vetterling, W. T., & Flannery, B. P., ed.
- Reid B. A. et al., 2010, *MNRAS*, 404, 60
- Sakharov A. D., 1966, *Soviet Journal of Experimental and Theoretical Physics*, 22, 241
- Sawangwit U., Shanks T., Abdalla F. B., Cannon R. D., Croom S. M., Edge A. C., Ross N. P., Wake D. A., 2011, *MNRAS*, 416, 3033
- Schlegel D. et al., 2011, *ArXiv e-prints*
- Schlegel D., White M., Eisenstein D., 2009, in *ArXiv Astrophysics e-prints*, Vol. 2010, *astro2010: The Astronomy and Astrophysics Decadal Survey*, p. 314
- Scoccimarro R., 2004, *Phys. Rev. D*, 70, 083007
- Seo H.-J. et al., 2010, *ApJ*, 720, 1650
- Seo H.-J., Eisenstein D. J., 2003, *ApJ*, 598, 720
- Seo H.-J. et al., 2012, *ArXiv e-prints*
- Seo H.-J., Siegel E. R., Eisenstein D. J., White M., 2008, *ApJ*, 686, 13
- Smith J. A. et al., 2002, *AJ*, 123, 2121
- Smith R. E., Scoccimarro R., Sheth R. K., 2008, *Phys. Rev. D*, 77, 043525
- Strauss M. A. et al., 2002, *AJ*, 124, 1810
- Sunyaev R. A., Zeldovich Y. B., 1970, *Ap&SS*, 7, 3
- Tegmark M., 1997, *Physical Review Letters*, 79, 3806
- Tucker D. L. et al., 2006, *Astronomische Nachrichten*, 327, 821
- Weinberg D. H., Mortonson M. J., Eisenstein D. J., Hirata C., Riess A. G., Rozo E., 2012, *ArXiv e-prints*
- Xu X., Padmanabhan N., Eisenstein D. J., Mehta K. T., Cuesta A. J., 2012, *MNRAS*, submitted
- York D. G. et al., 2000, *AJ*, 120, 1579
- Zaroubi S., Hoffman Y., Fisher K. B., Lahav O., 1995, *ApJ*, 449, 446
- Zel'dovich Y. B., 1970, *A&A*, 5, 84